JOURNAL OF AIRCRAFT
Vol. 43, No. 3, May–June 2006

Aero-Optic Performance of an Aircraft Forward-Facing Optical Turret

John E. Pond*
Analysis and Applications Associates, Inc., Huntsville, Alabama 35805
and
George W. Sutton†
SPARTA, Inc., Arlington, Virginia 22209

The results of three-dimensional calculations are presented for aero-optic analysis of an aircraft forward-facing optical turret. Computational-fluid-dynamics calculations, using a compressibility corrected k–ε turbulence model, defined the mean flow properties. Turbulence characteristics were obtained from a three-dimensional "g" law equation that yielded the variance of index-of-refraction fluctuations. The characteristic scale length of the correlation function of the index-of-refraction fluctuations was calculated. Strehl ratios and wave front distortion were computed for the mean flow and turbulence aberrations for four azimuth angles, 0, 45, 90, and 120 deg. For 90 and 120 deg azimuth, a portion of the beam passes through an open cavity with large-scale turbulence and nonuniform mean flow. For the mean flow, the Strehl ratio decreased to 0.001 at 90-deg azimuth after tip, tilt, and best focus were removed for a wavelength of 1.06 μm. The loss of Strehl as a result of turbulence was not as severe. Wind-tunnel measurements of optical path differences scale favorably to this work. In addition, instantaneous far-field intensity plots for instantaneous realizations of turbulence were constructed. A deformable mirror adaptive optics system might improve the Strehl ratio for the mean flow, but probably not for turbulence.

Nomenclature

a	=	aperture diameter
C	=	constant
D	=	turbulence structure function
F	=	focal distance
G	=	geometric matrix
g	=	scalar flow variable
I	=	intensity
J	=	Jacobian of coordinate transformation
k	=	wave number, $2\pi/\lambda$; turbulence kinetic energy
l'	=	turbulence integral scale size
M	=	Mach number
n'	=	rms index-of-refraction fluctuation
P_r	=	turbulence kinetic energy production rate
q	=	general field variable
R	=	gas constant
r	=	θf
S_q	=	source terms
t	=	time
U_i, u_i	=	velocity, amplitude
x_i	=	coordinate
β	=	Gladstone–Dale constant
Γ	=	mutual coherence function
γ	=	ratio of specific heats
ε	=	turbulence kinetic energy dissipation rate
θ_i	=	angles
λ	=	wavelength
μ	=	viscosity
ξ_i	=	coordinate
σ_k	=	Stanton number
τ	=	modulation transfer function
Φ	=	phase correlation function

Presented as Paper 2005-4779 at the AIAA 36th Plasmadynamics and Lasers Conference, Toronto, Canada, 6–9 June 2005; received 6 July 2005; revision received 15 September 2005; accepted for publication 25 October 2005.

*President. Senior Member AIAA.
†Senior Research Scientist. Honorary fellow AIAA.

I. Introduction

THIS effort reports calculations of aero-optic aberrations caused by the near-field nonuniform mean and turbulent flow about a forward-looking aircraft turret. This configuration is an alternative to the side-looking turret of the Airborne Laser Laboratory or the side open port on NASA's Stratospheric Observatory for Infrared Astronomy (SOFIA) 747SP aircraft. The compression of the mean flowfield causes optical aberrations as a result of the nonuniform index of refraction in the flow along the line of sight. This compression is caused by the aircraft velocity. A very slowly moving platform would not compress the air, nor would there be a temperature—and hence density—difference between the mean stream and the streamlines closest to the turret surface, which will be at the recovery temperature of the flow (for an adiabatic wall), and which drives the turbulence index-of-refraction fluctuations. The mean index-of-refraction nonuniformities cause lensing, resulting in tilt, defocusing, and wave-front distortion. The near-field turbulence introduced by boundary layers, shear layers, and separated flows, causes beam spreading, jitter, pointing errors, distorted wave front, and poor beam quality.

The turbulence was found by first writing a three-dimensional code to solve the Spalding scalar transport equation for the transport of the variance of index-of-refraction fluctuations using the grid generated for the computational fluid dynamics (CFD), and mean flow velocity, density, turbulent-kinetic-energy, and turbulent-kinetic-energy dissipation. From the solution of the stand-alone "g" law solver, the variance of index-of-refraction fluctuations and characteristic scale length were found. These quantities were used to find blur and optical distortion associated with the turbulence.

II. Analysis

A. Aircraft and Turret Geometry

The turret was defined using a sphere and cylinder as the basic shape. The turret diameter was assumed to be approximately 3.2 m,

and the length of the turret was 4.2 m from the turret nose to the point, where it intersects the aircraft on the upper centerline. The cavity (zone 2) was represented using a section of a cone for the rear surface, which intersected with the turret at the base of the cavity. The fuselage was scaled from a Heller 125:1 scale model of the Boeing 747 as a typical aircraft that might carry a large optical system. (The SOFIA is a B747SP.)

B. Computational Grid (Zone I)

The grid for (zone I) was generated using a FORTRAN code written specifically to define the three-dimensional grid around the fuselage and turret. The origin of the coordinate system was located at the nose of the turret (Fig. 1). Grid points were clustered near the surface by using stretching functions to give the necessary grid density near the body. The final grid (zone 1) used 73 grid points around the body (5.0-deg increments), 65 grid points down the body and 55 grid points away from the body, and is shown in Fig. 1. The boundary layer on the body surface was defined using a standard wall function approach, with a modified universal turbulent velocity profile, so that the first grid point away from the wall was located at the outer edge of the boundary layer. Adjustments were made during the CFD process to locate the first grid point the appropriate distance away from the wall. The grid in the cavity was generated using a second FORTRAN code to match the nodes with the nodes in the external grid (zone 1) at the zonal interface. Node points in zones 1 and 2 coincide. The meshing at the interface is shown in Fig. 2 on the turret outer surface. The cavity was defined by 15 grid points in the x direction, 17 grid points in the z direction, and 21 grid points in the y direction (around the turret). This allowed the interface to be a 15×21 grid. A plot of the surface grid is shown in Fig. 2.

C. Computational Fluid Dynamics

The finite difference Navier–Stokes code (FDNS)[1], developed by Engineering Sciences, Inc., was applied to solve the combined flowfield (zones 1 and 2). It is a fully conservative code that can be used to solve three-dimensional forms of the Navier–Stokes equations or two-dimensional planar, two-dimensional axissymmetric and other scalar transport equations using primitive variables and general multizone multiblock curvilinear coordinate mesh systems. Compressible or incompressible, laminar or turbulent flow problems can be solved using the pressure-based predictor/multicorrector solution algorithm. Finite difference approximations are employed to discreditize the transport equations on nonstaggered grid mesh systems. High-order (second- or third-order), upwind or central differencing schemes plus adaptive second-order and fourth-order dissipation terms were used to approximate the convective terms of the transport equations. Second-order central differencing schemes were used for the viscous and source terms of the governing equations. A pressure-based predictor/multicorrector solution procedure was employed to enhance velocity-pressure coupling and mass-conserved flowfield solutions at the end of each time step. The pressure-based method was suitable for all speed flow computations. A time-centered Crank–Nicholson time-marching scheme was used for the temporal discreditization for time-accurate solutions.

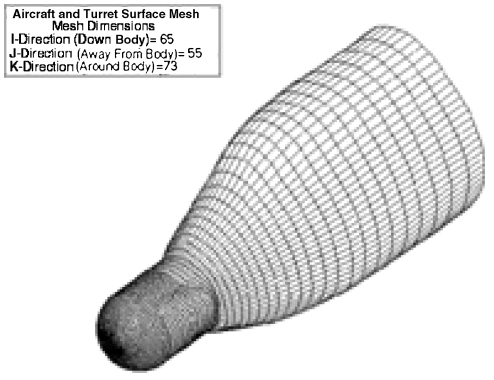

Fig. 1 Forward fuselage and turret surface nodes and mesh.

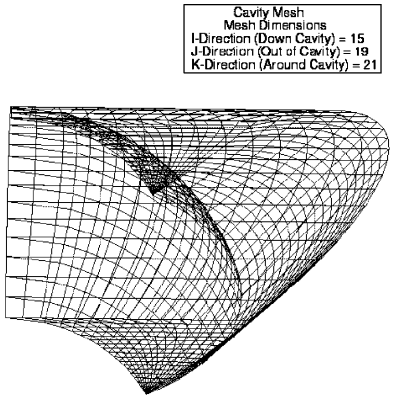

Fig. 2 Zone 1–zone 2 cavity surface mesh plot.

1. *Governing Equations*

The basic equations employed to define the flowfield are the Reynolds-averaged Navier–Stokes equations in curvilinear coordinates. A generalized form is written as follows[1]:

$$\frac{\partial(\rho q/J)}{\partial t} + \frac{\partial(\rho U_i q)}{\partial \xi_i} = \frac{\partial[\mu_{\text{eff}} G_{ij}(\partial q/\partial \xi_i)]}{\partial \xi_i} + S_q \qquad (1)$$

where J, U_i, and G_{ij} are the Jacobians of the coordinate transformation, contravariant velocity components, and geometrical matrices, respectively. They are given as

$$J = \frac{\partial(\xi, \eta, \zeta)}{\partial(x, y, z)}, \quad U_i = \frac{u_j}{J}\left(\frac{\partial \xi_i}{\partial x_j}\right),$$

$$\text{and} \qquad G_{ij} = \left(\frac{\partial \xi_i}{\partial x_k}\right)\left(\frac{\partial \xi_j}{\partial x_k}\right)\Big/ J \qquad (1a)$$

The effective viscosity $I_{\text{eff}} = (\mu + \mu_\tau)/\sigma_q$ is defined using the eddy viscosity μ_t concept, which was employed to model turbulent flow, and μ, the molecular viscosity of the flowing fluid. The q in the general equation represents field variables such as velocity u, v, internal energy (or enthalpy), individual species density, as well as the turbulence quantities to be solved for modeling eddy viscositie. S_q represents source terms for which detailed formulations can be found in standard references.[1] In addition, ρ is density, and ξ_i are the computational coordinates.

2. *Turbulence Transport Model for CFD*

Turbulence modeling for the CFD was based on the eddy-viscosity concept, which was defined by the turbulent kinetic energy k and turbulent-kinetic-energy dissipation rate ε in the two-equation k-ε model. The FDNS code has two compressibility corrected models: the first was the k-corrected model,[2] where an additional term was added to the k equation, and the second was the ε-corrected model,[3] where the dissipation was rescaled by a function depending on the local flow Mach number. Eddy viscosity for this study was defined using the k-corrected turbulent Mach-number compressibility correction shown in Eqs. (2) and (3) for the mass-weighted turbulence equations for turbulence kinetic energy k and its dissipation rate ε.

$$\frac{\partial \bar{\rho} k}{\partial t} + \frac{\partial(\bar{\rho} U_j k)}{\partial \xi_j} = \frac{\partial U_i}{\partial \xi_j}\left(\frac{\mu_t}{\sigma_k}\frac{\partial k}{\partial \xi_j}\right) + \rho(P_r + \rho) - \rho M_t \varepsilon \quad (2)$$

$$\frac{\partial \bar{\rho} \varepsilon}{\partial t} + \frac{\partial(\bar{\rho} U_j \varepsilon)}{\partial \xi_j} = \frac{\partial U_i}{\partial \xi_j}\left(\frac{\mu_t}{\sigma_\varepsilon}\frac{\partial \varepsilon}{\partial \xi_j}\right) + \rho\frac{\varepsilon}{k}(C_1 P_r - C_2 \varepsilon) \quad (3)$$

In the preceding equations, the standard model constants C_1 and C_2 are set to 1.43 and 1.92, respectively. The turbulence-kinetic-energy

Table 1 Freestream conditions at 38,500 ft and Mach no = 0.76

Condition	Value
Pressure	20,250.40 N/m^3
Temperature	216.6 K
Density	0.32552 kg/m^3
Velocity	244.57 m/s
Reynolds no.	5.1533×10^7/m

production rate was written as

$$P_r = (\mu_t/\rho)\left[2(u_x + v_y + w_z) + (v_x + u_y)^2 + (w_y + v_z)^2 + (u_z + w_x)^2 - \tfrac{2}{3}(\nabla u)^2\right] \quad (4)$$

and the local turbulence Mach number is

$$M_t = \sqrt{k/\gamma RT} \quad (5)$$

The turbulent viscosity is defined next, with the constant $C_\mu = 0.09$ and

$$\mu_t = C_\mu \rho k^2 / \varepsilon \quad (6)$$

3. Freestream and Boundary Conditions

For an altitude of 38,500 ft and Mach number = 0.76, the freestream atmospheric properties are shown in Table 1.

The freestream values of turbulent kinetic energy k and the turbulent kinetic energy dissipation ε are input values required for turbulent CFD analysis. Freestream atmospheric turbulence level is typically very low with a value for the turbulent velocity fluctuations u' on the order of $\frac{1}{2}$ % of the freestream velocity. Therefore, the freestream value of the turbulent kinetic energy was set to $k = u'^2 = (0.005U_{\text{inf}})^2$. The value of the freestream turbulent kinetic energy dissipation was set so that the resulting freestream turbulent viscosity was less than or near the laminar viscosity. This approach guaranteed correct low turbulence effects in the free atmosphere. No-slip wall boundary conditions were imposed at the surface boundaries with a wall temperature T_w fixed at the recover temperature given by $T_w/T_0 = 1.07$.

III. Results

At these conditions, the flow remained attached over the turret with no separation noted at the turret-fuselage intersection. Pressure and density disturbances were shown to exist upstream to the extent of the grid, which was 27 m forward of the turret nose. Large compression "bubbles" were shown on the turret with an expansion at the sphere-cylinder intersection followed by a compression at the turret-fuselage intersection and an expansion above the cockpit window and fuselage sides. The flow in the cavity behind the turret ball was shown to enter downstream near the fuselage and then rotate inside the cavity. A large velocity component was noted in the upward direction, caused by the angle-of-attack effect, which causes a higher pressure in the lower portion of the cavity and a large upward component of flow to emerge from the top of the cavity. This causes turbulence downstream, which impinges on the fuselage side.

In Fig. 3 the density field is shown for a plan view at midplane. This view shows the general nature of the flowfield that consists of a compression region in front of the vehicle with compression bubble in the nose region. The flow is then compressed by the fuselage from the turret-fuselage intersection to top of the aircraft, above the cockpit, and also on the underside about the same station as the expansion above the cockpit. A compression is evident at the turret-aircraft intersection.

The surface velocity vectors (one node point above the surface) and streamlines are shown in Fig. 4. A vortex leaves the cavity and then trails downstream, impinging on the side of the aircraft. The flow inside the cavity had a significant upward component that was caused by the positive incidence of the turret (2.5 deg). A higher pressure existed on the lower portion of the cavity rear surface, inducing a bottom-to-top pressure gradient.

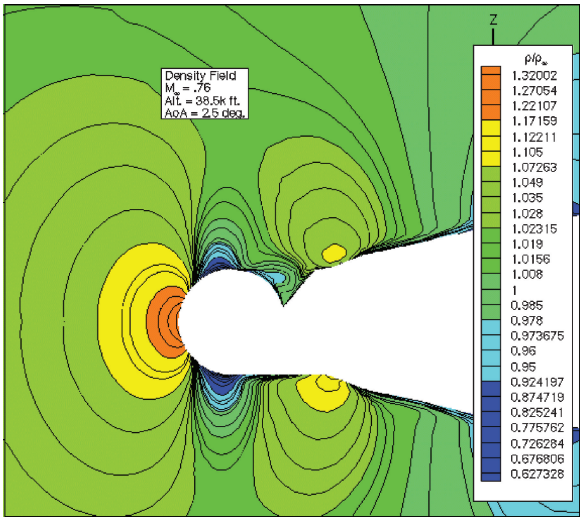

Fig. 3 Plan view of turret and aircraft density field.

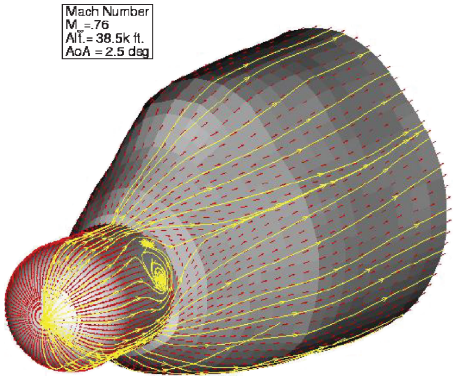

Fig. 4 Surface velocity and streamlines.

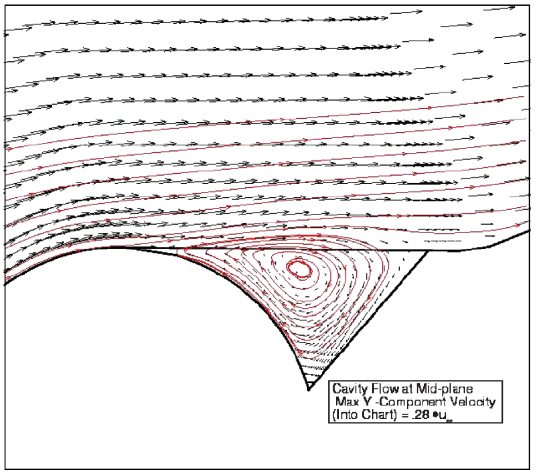

Fig. 5 Turret cavity recirculation flow pattern.

A. Cavity Flow Results (Zone 2)

In Fig. 5, recirculation is shown on the rear side of the turret ball. At the midplane the flow impinges on the rear of the cavity increasing the pressure and causing the flow downward and then upward behind the turret ball. This causes a slight bulge in the external stream lines. An important feature of the flow not shown in this view was a strong velocity component upward from the lower

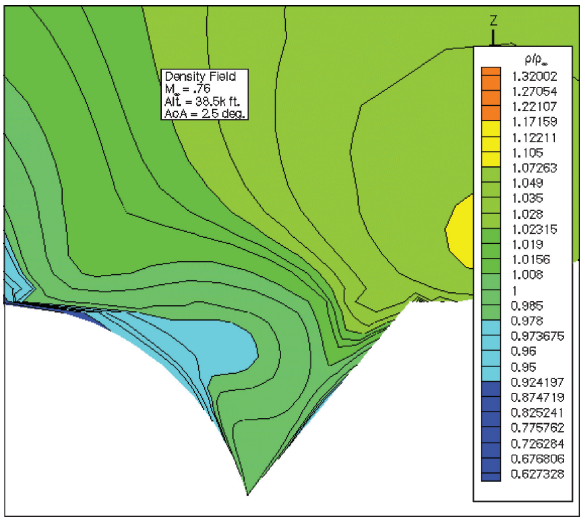

Fig. 6 Turret cavity mean density field.

surface of the cavity, upward. The highest value of this component (y component) was computed to be 0.28 of the freestream velocity or 68.48 m/s. In Fig. 6 the density field associated with the cavity is shown. Here, the density at the rear of the cavity was the highest, where the external flow impinges, and the lowest density was at the rear of the turret ball. Flow impinges on the lower surface as a result of the 2.5-deg angle of attack. This causes the high-pressure region and resulting upward flow component in the cavity.

B. Turbulence Characterization for Aero-Optics

The interface between CFD and aero-optics provides a method to compute the variance of the index-of-refraction fluctuations and the turbulence length scale from time-mean flowfield solutions of the CFD (FDNS) code. The model chosen[4] was based on a transport equation for the variance of fluctuations of a passive scalar quantity that has the same form as the transport equations for turbulent kinetic energy and dissipation.

1. *Variance of Index-of-Refraction Fluctuations; 'g' Law Formulation*

The index of refraction is related to the density through the Gladstone–Dale relation

$$n = 1.0 + \beta_m \rho \tag{7}$$

where β_m is the Gladstone–Dale constant for the mixture (air). The variance of the index-of-refraction fluctuations, $g = \langle (n')^2 \rangle$, was computed using the transport equation[5]

$$\frac{\partial(\rho g)}{\partial t} + \frac{\partial \rho u g}{\partial x} + \frac{\partial \rho v g}{\partial y} + \frac{\partial \rho w g}{\partial z} = \frac{\partial}{\partial x}\left[\frac{\mu_l + \mu_t}{\sigma_g}\frac{\partial g}{\partial x}\right] + \frac{\partial}{\partial y}\left[\frac{\mu_l + \mu}{\sigma_g}\frac{\partial g}{\partial y}\right] + \frac{\partial}{\partial z}\left[\frac{\mu_t + \mu_l}{\sigma_g}\frac{\partial g}{\partial z}\right] + C_{1g}\mu_t\left[\left(\frac{\partial n}{\partial x}\right)^2 + \left(\frac{\partial n}{\partial y}\right)^2 + \left(\frac{\partial n}{\partial z}\right)^2\right] - C_{2g}\frac{\rho g \varepsilon}{k} \tag{8}$$

Under the assumption of equilibrium, in which the convection and diffusion terms of the transport equation for $\langle (n')^2 \rangle$ are assumed to be equal, the production and dissipation terms are then set equal such that

$$C_{1g}\mu_t\left[\left(\frac{\partial n}{\partial x}\right)^2 + \left(\frac{\partial n}{\partial y}\right)^2 + \left(\frac{\partial n}{\partial z}\right)^2\right] = C_{2g}\frac{\rho g \varepsilon}{k} \tag{9}$$

and at high Reynolds numbers (which is the case for the laser turret and aircraft at 38,500 ft and Mach 0.76) the turbulent viscosity is

$$\mu_t = C_\mu \rho k^2 / \tau \tag{10}$$

where C_μ is an empirical constant. Substituting in the expression for μ_t, k, and ε, we obtained for the upstream boundary condition

$$\langle (n')^2 \rangle = C_{1g}\mu_t\left[\left(\frac{\partial n}{\partial x}\right)^2 + \left(\frac{\partial n}{\partial y}\right)^2 + \left(\frac{\partial n}{\partial z}\right)^2\right] \tag{11}$$

where $C_{1g} = 2.80$, $C_{2g} = 1.40$, and $C_\mu = 0.09$. An upwinding relaxation scheme was used to drive the residuals at each cell on the CFD grid to machine zero. The solution is depicted in Fig. 7 for the plan view of the aircraft turret. The cavity area causes the turbulence to extend further into the external flow.

2. *Characteristic Length Scale*

The turbulent length scale was calculated from the expression for the turbulent dissipation in equilibrium[5]

$$l' = k^{\frac{3}{2}} / \varepsilon \tag{12}$$

where the turbulent kinetic energy k and the turbulent kinetic energy dissipation ε are taken directly from the FDNS solution. The plan-view distribution is shown in Fig. 8 in which the characteristic scale length in the cavity was nearly 30 cm; however, the line of sight for the 120-deg look angle case does not pass through the highest values. The extent of the turbulence is shown to be somewhat greater than the thickness of the boundary layer over the turret.

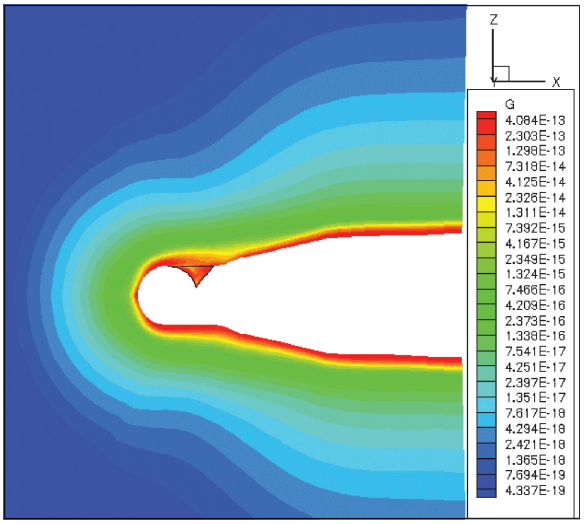

Fig. 7 Aircraft-turret variance of index of refraction.

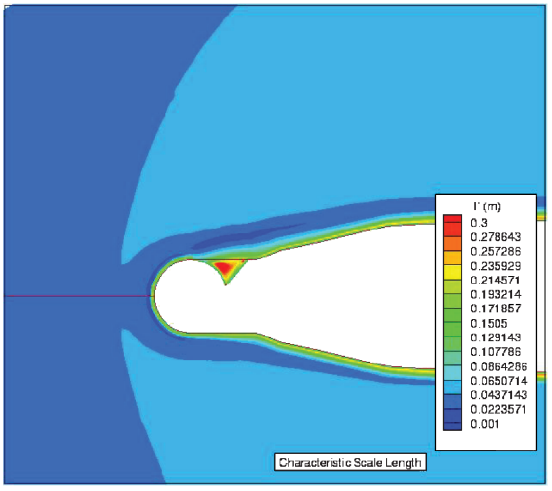

Fig. 8 Distribution of the turbulence scale size, plan view.

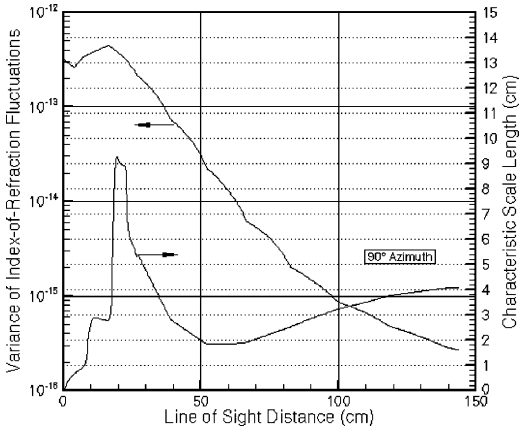

Fig. 9 Turbulence characterization for 90-deg line of sight.

3. Line-of-Sight Turbulence

Results of these calculations, the variance of index of refraction, and characteristic scale length were extracted from the fields (zones 1 and 2). For each, the turbulence properties were taken for approximately 150-cm distance from the turret to a point where turbulence levels no longer caused significant scattering. To assess the magnitude of the turbulence level, the fluctuating density can be computed from the variance of index of refraction by the following expression, where ρ is the local density:

$$\rho'/\rho = g^{\frac{1}{2}} \Big/ \rho\beta_{G-D} \tag{13}$$

The line-of-sight turbulence characteristics for the 90-deg azimuth angle is shown in Fig. 9.

IV. Aero-Optics Results

A. Mean Flow Aberrations

The optical effects of the three-dimensional mean flowfield were determined by computing optical path differences by passing rays through the CFD grid. As an initially plane wave propagates through the mean flow, of varying refractive index, the wave front becomes distorted and tilted, which results in pointing and focusing errors. Using the mean density field and the Gladstone–Dale relationship to find the mean index of refraction, the optical path difference (OPD) was found over the aperture by projecting a bundle of rays to the aperture, through the CFD grid. A plane, perpendicular to the beam, was defined at a location in the freestream near the outer boundary of the CFD grid, where little disturbance to the mean flow was expected. A bundle of rays was then projected parallel to the line of sight through the mean flow to the aperture. Integrating the index of refraction along each ray and subtracting the freestream index of refraction defines the OPD as follows:

$$\mathrm{OPD}(x', y') = \int_0^L \sum \rho(x', y')\beta \, \mathrm{d}s - \int_0^L \rho_{\mathrm{fs}}\beta_{\mathrm{fs}} \, \mathrm{d}s \tag{14}$$

where β is the Gladstone–Dale constant, and ρ_{fs} and β_{fs} are the freestream density and Gladstone–Dale constant, respectively. A map of the optical path difference over the aperture from this procedure can be interpreted as the phase errors produced by the mean flow. No contribution to the OPD was taken inward of the outer surface of the aperture. In Fig. 10 the OPD for the bundle of rays, 51×51, is shown for the 120-deg azimuth with tip, tilt, and best focus removed.

B. Mean Flow Optical Path Difference Results

The raw optical path difference consisted of almost concentric circular patterns caused by the lensing effect of the compression bubble ahead of the turret shown in Fig. 3. There was a downward offset caused by the 2.5-deg angle of attack of the aircraft.

The mean flow immediately upstream of the turret (0-deg azimuth angle) was found to have a nonuniform index-of-refraction field and acted much like a large lens. The mean index-of-refraction field at the 45-deg azimuth angle was shown to have large gradients in the downstream direction, which implied a large uncorrected pointing error. The 90-deg azimuth angle showed the effect of a downstream portion of the aperture being in the cavity and separated flow region. The 120-deg azimuth angle showed large wave-front distortion gradients. From the OPD, in best focus, the far-field intensity was computed from the Fourier transform of the OPD, represented as a phasor, to yield the electric field and then determined the intensity from its modulus. Using this procedure, Strehl ratio and wave-front distortion were computed for the mean flow effects. The electric field was computed from the following expression[6]:

Table 2 Strehl ratio for mean flow aberration, 1.06 μm

Az. angle, deg	σ_{rms}, μm	Strehl ratio for 1.060-μm wavelength
0	0.05595	0.8958
45	0.28888	0.05331
90	0.44150	0.00106
120	0.32870	0.02242

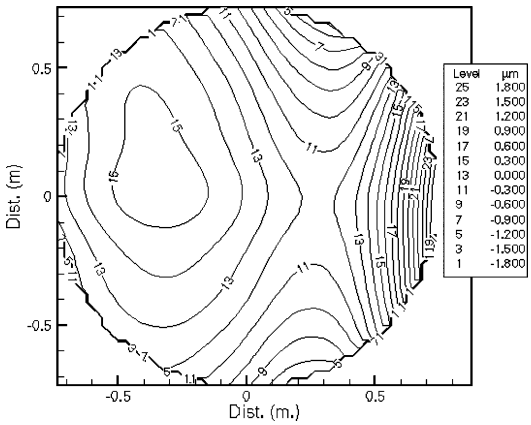

Fig. 10 Residual OPD with tip and tilt removed, for best focus for 90-deg azimuth.

$$U(\theta_x, \theta_y) = \int_{-D/2}^{D/2} \int_{-\sqrt{(D/2)^2 - x^2}}^{\sqrt{(D/2)^2 + x^2}} \exp\left[i2\pi(opd)/\lambda\right] \times \exp[-i2\pi(\theta_x x + \theta_y y)/\lambda] \, \mathrm{d}x \, \mathrm{d}y \tag{15}$$

where θ_x, θ_y are angles measured from the central ray and the limits of integration are over the aperture diameter, 1.5 m. The intensity was then found by computing the modulus as shown next:

$$I_m(\theta_x, \theta_y) = U(\theta_x, \theta_y)U^*(\theta_x, \theta_y) \tag{16}$$

From the intensity, Strehl loss, the rms wave-front distortion for the mean flow effects can be found by $I_m(0, \theta)$. The rms wave-front distortion was computed from the following expression:

$$\sigma_{\mathrm{rms}} = \sqrt{\sum_{i=1}^{N} \mathrm{OPD}'''^2} \Big/ N \tag{17}$$

where N is the number of OPD values within the aperture. The Strehl ratio for the nonuniform mean flow was then approximated by the Maréchal approximation[7] for $I_m(0, 0)$ of Eq. (21).

$$SR = \exp -[(2\pi/\lambda)\sigma_{\mathrm{rms}}]^2 \tag{18}$$

The rms wave-front distortion and Strehl ratio for the four look angles are given in Table 2.

In general, the pointing error (tip and tilt) were removed by subtracting the best-fit plane. In addition focusing errors have been

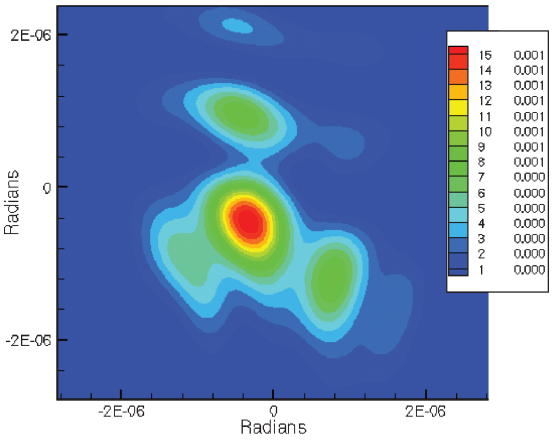

Fig. 11 Far-field intensity for $\lambda = 1.060\ \mu$m for azimuth angle = 90 deg.

removed by subtracting the best-fit paraboloid. The remaining rms wave-front distortion is shown in Fig. 10 for 90-deg azimuth angle. The remaining rms wave-front distortion was 0.4415 μm and yielded a Strehl ratio of 0.00106 for a wavelength of 1.060 μm. For the 0-deg azimuth angle, reasonable focus was achieved, and a Strehl ratio of approximately 0.90 with some energy dispersed to secondary lobes and the outer cusps filled. The 45-deg look angle shows a low Stehl ratio caused by the out-of-focus condition with energy dispersed. The 90-deg look-angle case shows the lowest Strehl ratio because of the out-of-focus condition that was caused by a large amount aperture being in the attached flow while the downstream portion was in the separated region. The 120-deg case shows low Strehl ratio because of the large portion of the aperture being in the separated cavity flow and the associated nonuniform density field. The farfield intensity pattern for 90-deg azimuth angle is shown in Fig. 11 for the wavelengths of 1.060-μm wavelength. For a shorter wavelength, say 0.53 μm, the Strehl ratio would be the fourth power of the SR for 1.06 μm.

C. Turbulence Aero-optic Methodology

For the flowfield, consisting of air $\langle (n')^2 \rangle$, was obtained from Eq. (8). Following experimental data,[6,7] the exponential correlation function of the refractive index fluctuation was used for these calculations as most realistic. The exponential function is given by

$$B_n = \langle n'^2 \rangle \exp -(x/l') \tag{19}$$

where x is the distance between two points in the turbulent medium. The turbulence length scale l' is the integral scale size, defined as

$$\int_{.0}^{\infty} e^{-x/l'}\, \mathrm{d}x$$

The basic quantity that was calculated was the focal plane intensity profile $I(\theta)$, as a function of angular radius, $\theta = r/f$, from the central axis. Here, the small-angle approximation $\theta = \sin\theta = r/f$ is quite precise for the small image blur being considered. From $I(\theta)$, Strehl ratio, the encircled energy curve and, as will be seen, the wave-front distortion can be determined. The intensity distribution in the presence of turbulence is given by[8]

$$I(\theta) = \frac{k^2}{2\pi f^2} \int_0^{2a} r'\, \mathrm{d}r' J_0\left(\frac{kr'}{f} r'\right) \Gamma(L, r') \tau_a \left(\frac{r'}{a}\right) \tag{20}$$

Here, $k = 2\pi/\lambda$, where f is the focal distance, a is the aperture radius, J_0 is the zero-order Bessel function, and r' is the separation distance between two points on the aperture and $\theta = r'/f$. The function τ is the modulation transfer function (MTF) of the aperture, given by

$$\tau_a = 2a^2 \left[\cos^{-1}\left(\frac{r'^2}{2a}\right) - \frac{r'}{2a}\left(1 - \frac{r'^2}{4a^2}\right)^{\frac{1}{2}} \right] \quad \text{for} \tag{21}$$

and $= 0$ for $r' < 0$. In Eq. (20), $\Gamma(L, r')$ is the mutual coherence function and is given in terms of the wave structure function $D(L, r')$ by

$$\Gamma(L, r') = \exp[-D(L, r')/2] \tag{22}$$

For the present case for the exponential correlation function B_n, the wave structure function turns out to be

$$D(L, r') = \int_0^L 4k^2 \langle n'^2 \rangle l' \left[1 - \left(\frac{r'}{l'}\right) K_1 \left(\frac{r'}{l'}\right) \right] \mathrm{d}s \tag{23}$$

where ds is the incremental distance along the propagation path, K_1 is the modified Bessel function of the second kind, and n' and l' are functions of s. The blur circle calculation shows the far-field image with filled cusps and reduced central lobe, and the Strehl ratio for 90-deg case was 0.7379 for the 1.060-μm wavelength. Instantaneous blur circles are shown later.

D. Instantaneous Realizations for Turbulence Effects.

Turbulence in the mean flowfield, and particularly in the boundary, shear layer, and separated portions of the flow was assumed to be "frozen" as opposed to ensemble averaged. The net result of looking through the frozen or nearly frozen turbulence is that the centroid of the far-field intensity moves, in an uncorrelated manner, with each realization, causing jitter. As the level of turbulence is increased, the far-field intensity becomes more distorted, and the centroid movement increases. In cases where the turbulence level is severe, the far-field intensity becomes completely dispersed.

The shape to the correlation function describing the index-of-refraction fluctuation was taken to be exponential, in agreement with experimental measurements, as mentioned earlier. Instantaneous realizations of the phase aberrations were found by determining the index-of-refraction covariance and phase correlation using the exponential correlation for the turbulence. Using the variance of the index-of refraction fluctuations found from the solution to the g equation, discussed earlier, and the characteristic length scale distribution, the phase correlation function for the exponential refractive index correlation is given by

$$B(\rho) = 2k^2 \int_{s=0}^{L} \langle n'^2(s) \rangle \int_{x=0}^{\infty} \exp\left[\frac{\rho^2}{l'^2(s)} + \frac{x^2}{l'^2(s)} \right]^{\frac{1}{2}} \mathrm{d}x\, \mathrm{d}s \tag{24}$$

where $k = 2\pi\lambda$ and $\rho = (y^2 + z^2)^{1/2}$. By suitable transformation, the inner integral is exact. The phase correlation can then be written as follows[9]:

$$\Phi(\rho) = 2k^2 \int_{s=0}^{L} \left\langle n'^2(s) \right\rangle \rho K_1 \left[\frac{\rho}{l'(s)} \right] \mathrm{d}s \tag{25}$$

where K_1 is the first-order modified Bessel function of the second kind. The phase power spectral density (PSD) was determined from the Fourier transform of the phase correlation. From the PSD, random phase screens were generated using an independent Gaussian random variable having a zero mean and unit variance, resulting in the phase PSD uniformly distributed between 0 and 2π. The PSD was found, from the Fourier transform of the phase correlation resulting in a unique random phase screen, with spatial frequency properties given by the PSD. The phase screen was then computed from the following Fourier integral, in which z is a Gaussian distributed random number[10]:

$$\Phi(x, y) = \int \int_{-\infty}^{+\infty} \left| P(k_x\, k_y) \right|^{\frac{1}{2}} z(k_x, k_y) e^{i(k_x x + k_y y)}\, \mathrm{d}k_x\, \mathrm{d}k_y \tag{26}$$

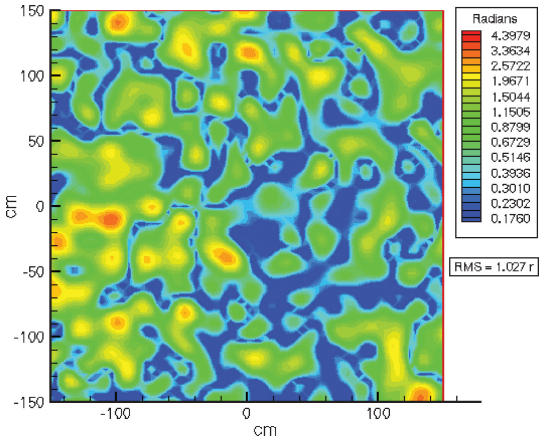

Fig. 12 Instantaneous phase screen (azimuth = 120 deg, $\lambda = 1.060\ \mu$m).

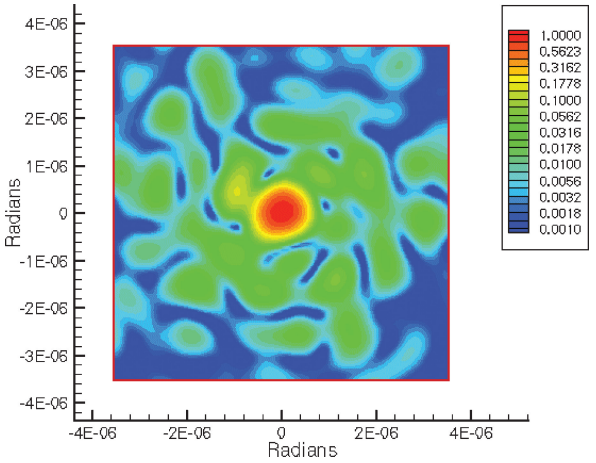

Fig. 13 Instantaneous far field (azimuth = 120 deg, $\lambda = 1.060\ \mu$m).

E. Instantaneous Phase Screens.

Instantaneous phase screens were computed for each of the four azimuth angles and 1.060-μm wavelength. A plot of a phase screen is shown in Fig. 12 for 1.060 μm for the 120-deg azimuthal angle.

The far-field instantaneous realizations were obtained by first calculating the electric field by taking the Fourier transform of the random screen, represented as a phasor, shown next:

$$U(\theta_x, \theta_y) = \int\int_{-\infty}^{+\infty} e^{i\Phi} \exp\left[-i\frac{2\pi}{\lambda}(\theta_x x + \theta_y y)\right] \mathrm{d}y\, \mathrm{d}x \quad (27)$$

and calculating the intensity by finding its modulus, shown here:

$$I(\theta_x, \theta_y) = U(\theta_x, \theta_y) U^*(\theta_x, \theta_y) \quad (28)$$

Autocorrelations of the random phase screens were compared to the original phase correlation and found to be in good agreement. Far-field realizations, normalized to 1.0 at the maximum intensity, computed from an instanteous phase screen in Fig. 13 for 1.060 μm. This plot show much of the energy has been dispersed, and the central lobe was somewhat broken. Here the ensemble-averaged Strehl ratio is 0.3818.

V. Discussion

As a general case, propagation lengths through the disturbed mean flow are large, causing significant optical aberration, lensing effects, pointing errors, and steep wave-front gradients at the aperture. The 0-deg azimuth case mean flow wave-front errors had a relatively low rms wave-front error. For the 45-deg azimuth case, a very large pointing error was found over the aperture, caused by high-density flow on the most forward portion of the aperture and a much lower density on the downstream segment. Wave-front errors remained after subtracting the best-fit paraboloid, considerable distortion remained, and Strehl ratio was low. The 90-deg case showed the effect of the most forward portion of the aperture being in the upstream, attached flow, whereas downstream, the aperture was in the separated flow of the cavity. The density disparity in these two regions made focusing errors impossible to remove, and the resulting Strehl was found to be very low. Finally, the wave-front errors for the 120-deg case were again difficult to improve to any extent because of the steep and somewhat random gradients; thus, a very low Strehl ratio was calculated. Strehl ratio and rms wave-front distortion are shown in Table 3. The next step should be to include the improvements achievable with adaptive optics, by subtracting higher-order Zernike polynomials from the OPD results and reevaluating the resulting Strehl ratio.

Table 3 Summary: turbulent and mean flow Strehl ratio and wave-front distortion

	$\lambda = 1.060\ \mu$m			
Azimuth	0 deg	45 deg	90 deg	120 deg
Turbulence				
SR	0.8926	0.8487	0.7379	0.3818
σ_{rms}, r	0.3386	0.4170	0.5582	1.0267
Mean flow				
SR	0.8958	0.0533	0.0010	0.0224
σ_{rms}, μm	0.0559	0.2888	0.4415	0.3287

Table 4 Comparison with wind-tunnel results[12]

Optical path difference	Present results	Scale up from wind tunnel
Mean flow OPD over aperture, μ	0.442	0.374
Turbulence rms OPD at 90°, μ	0.0942	0.0501

Turbulence aberrations for azimuth angles of 90 deg or less are relatively small because of short propagation path distances through turbulence. Maximum turbulent density fluctuations are on the order of 2.0% and relate to a low variance of index-of-refraction fluctuation. This was a direct result of a relatively low Mach number, 0.76. Aberrations for the 120-deg azimuth angle case show a significant turbulence effect, as a result of a greater propagation distance through turbulence and a larger turbulence characteristic scale length in the cavity. A summary of the Strehl ratio and wave-front distortion for the turbulence induced effect is shown in Table 3. The combined effects of mean flow and turbulence can be combined through the products of their MTFs. Because the turbulence is uncorrelated with the mean flow, an estimate of the combined *SR* can be obtained from the product of their respective Strehl ratios, in the Maréchal approximation. The next step should be the integration of the aperture distribution of the turbulence instead of only along the chief ray.[11]

The calculation results are compared to wind-tunnel results on a dome-cylinder.[12] The latter flow was at right angles to the axis of the sphere-cylinder; to make a comparison, the 90-deg angle results were used. The wind tunnel was scaled to flight by freestream density, the square of the Mach number, geometry, and wavelength. The results are shown in Table 4, for scaling up to the present study. It is seen that the results for the mean flow compare favorably, in spite of the difference in the flow direction. The rms OPD from the wind tunnel is over the entire aperture, which is at an angle to the flow, and so it should be slightly lower than turbulence of the current work, as shown in Table 4.

The nonuniform mean flow effects could be eliminated by using a conical turret. Mean flow density nonuniformity in an open cavity is similar to a base flow or bluff-body wake, characterized by spatial velocity nonuniformity and hence a nonuniform density. This situation can only be eliminated by removing separated flow. For the rearward beam angle, a streamlined aerodynamic window might have more potential. The next step should be modeling the

improvements that can be attained by means of an adaptive optics to reduce the optical aberrations caused by the mean flow effects. For the turbulence adaptive optics, corrections with deformable mirrors are doubtful because of the turbulence high spatial and temporal frequencies. Turbulence effects can be reduced by lowering the freestream Mach number. The turbulence characteristic length scale can be reduced by reducing the characteristic length of the turret, aircraft, or cavity.

References

[1]Wang, T., and Chen, Y. S., "A Unified Navier–Stokes Flowfield and Performance Analysis of Liquid Rocket Engines," AIAA Paper 90-2994, 1990.

[2]Sarkar, S., Erlebacher, G., Huyssaini, M. T., and Kreiss, H. O., "The Analysis and Modeling of Dilitational Terms in Compressible Turbulence," ICASE, Rept. 89-79, Hampton, VA, 1989.

[3]Zeman, O., "Dilitational Dissipation: The Concept and Application in Modeling Compressible Mixing Layer," *Physics of Fluids*, Vol. A2, 1990, pp. 178–185.

[4]Spalding, D. B., "Concentration Fluctuations in a Round Turbulent Free Jet," *Chemical Engineering Science*, Vol. 26, Jan. 1971, pp. 95–107.

[5]Smith, R., Truman, C., and Masson, B., "Predictions of Optical Phase Degradation Using a Turbulent Transport Equation for the Variance of Index-of-Refraction Fluctuations," AIAA Paper 90-0250, Jan. 1990.

[6]Sutton, G. W., "Aero-Optical Foundations and Applications," *AIAA Journal*, Vol. 23, No. 10, 1885, pp. 1525–1537.

[7]Sutton, G. W., "Effect of Turbulent Fluctuations in an Optically Active Fluid Medium," *AIAA Journal*, Vol. 7, No. 11, 1969, pp. 1737–1743.

[8]Ishimaru, A., *Wave Propagation and Scattering in Random Media*, Vol. 2, Academic Press, New York, 1978, p. 303.

[9]Sutton, G. W., Pond, J. E., and Hwang, Y., "Phase Aberrated Instantaneous Target Realizations due to the Coolant over an Optical Window in Hypersonic Flight," AIAA/BMDO, Paper 4–6, Washington, DC, July 1994.

[10]Kathman, A. D., Brooks, L. C., Kalin, D. A., and Clark, R. L., "A Time-Integrated Image Model for Aero-Optic Analysis," AIAA Paper 92-2793, 1992.

[11]Sutton, G. W., "The Effect of Inhomogeneous Turbulence on Imaging Through Turbulent Layers," *Applied Optics*, Vol. 33, No. 18, June 1994, pp. 3972–3973.

[12]Gordeyev, S., Hayden, T., and Jumper, E. J., "Aero-Optical and Hot-Wire Measurements of the Flow Around the Hemispherical Turret With a Flat Window," AIAA Paper 2004-2450, June 2004.